

Article

Axial Compression Behaviour and Modelling of Pultruded Basalt-Fibre-Reinforced Polymer (BFRP) Tubes

Chuntao Zhang ^{1,2,*} , Yu Chen ¹ and Mei Dou ³

¹ School of Civil Engineering and Architecture, Southwest University of Science and Technology, Mianyang 621010, China; chenyu0616@126.com

² Shock and Vibration of Engineering Materials and Structures Key Laboratory of Sichuan Province, Mianyang 621010, China

³ China Southwest Architectural Design and Research Institute Corporation, Ltd., Chengdu 610000, China; doumei0417@126.com

* Correspondence: chuntaozhang@swust.edu.cn

Abstract: Laminated fibre-reinforced polymer (FRP) tubes are increasingly used as compression members in large-span spatial structures due to their high bearing capacity, corrosion resistance, and superior stability compared to high-strength steel pipes. In this study, axial compression tests were conducted on slender BFRP tubes to evaluate their compression characteristics as compression members. The results indicated that BFRP tubes exhibited three distinct failure modes, namely local failure, critical failure, and buckling failure. Overall, buckling was identified as the primary mode of failure under compression. The stress–strain curves of BFRP tubes were characterized by three stages, including elastic, elastic-plastic, and plastic stages. To enable design-oriented approaches, two three-stage theoretical models for BFRP tubes were developed through experimental data analysis. The models predicted the stress–strain curves and the load-lateral deflection curves, taking into account the post-peak softening behaviour of the stress–strain curves. Comparisons between the test results and the predictions calculated using the proposed models indicated that they were in good agreement.

Keywords: fibre-reinforced polymer; axial compression test; overall buckling; stress–strain model; load-lateral deflection model



Citation: Zhang, C.; Chen, Y.; Dou, M. Axial Compression Behaviour and Modelling of Pultruded Basalt-Fibre-Reinforced Polymer (BFRP) Tubes. *Buildings* **2023**, *13*, 1397. <https://doi.org/10.3390/buildings13061397>

Academic Editor: Oldrich Sucharda

Received: 26 April 2023

Revised: 22 May 2023

Accepted: 24 May 2023

Published: 27 May 2023



Copyright: © 2023 by the authors. Licensee MDPI, Basel, Switzerland. This article is an open access article distributed under the terms and conditions of the Creative Commons Attribution (CC BY) license (<https://creativecommons.org/licenses/by/4.0/>).

1. Introduction

Large-span spatial structures have garnered significant attention; however, the primary components of such structures currently comprise steel structures and lightweight maintenance structures [1–4]. The cross-sectional size of the structural member increases with an increase in the span of large-span spatial structures, which increases the weight and steel consumption of the structure [5]. Therefore, investigation on lightweight and high-strength materials is crucial to replace steel members in large-span spatial structures. There are multiple axially compressed rods in large-span spatial structures, and their instability is a critical mode of failure of large-span spatial structures [6–8]. Fibre-reinforced polymer (FRP) tubular compression members have exceptional properties such as lightweight and high strength. Additionally, they have good corrosion resistance and the production of some types of fibres is environmentally friendly [9–12]. They fulfil the requirements of mechanical properties, architectural design, and environmental protection of compressed rods in large-span spatial structures. Therefore, it is necessary to investigate the compressive performance of FRP tubes.

Multiple studies have been conducted on FRP columnar components. These studies cover three main areas, concrete columns confined with FRP [13–16], FRP columns [17–20], and hybrid FRP columns [21–24]. FRP column members are defined as members that primarily experience axial loading and are fabricated solely using FRP [25]. The mechanical

properties of FRP columns with diverse cross-sections have been studied by researchers utilizing experimental, numerical, and analytical methods. Zureick and Scott (1997) [26] performed a compression test on 24 pultruded FRP box and I-shaped sections with slenderness ratios between 36 and 103. Through analysis of the buckling behaviour and critical load of the specimens, they proposed a reduction factor to estimate the lower-limit value of the global buckling critical load. Qian et al. (2008) [27] conducted compression tests on five circular FRP tubes with external diameters, thicknesses, and lengths of 41.2 mm, 3.6 mm, and 120 mm, respectively. The mechanical properties of four groups of FRP tubes with slenderness ratios between 35 and 90 were determined under axial compression to investigate instability. Godat et al. (2013) [28] studied the axial behaviour of FRP members with angular, square, and rectangular sections having slope ratios from 12 to 65, to predict the failure mode. They also used the Perry formula to predict the buckling load of FRP pipes under axial compression. Chao Wu and Jie Tian (2022) [29] conducted an experimental and theoretical investigation of FRP channel sections subjected to axial compression, covering a range of slenderness ratios from 30 to 112. As the column length increased, they noticed that FRP channel sections experienced three distinct modes of failure: crushing of the section, local buckling, and global buckling. Although multiple studies have investigated the compression behaviour of FRP columns with different cross-sections, these studies have only examined a limited range of aspect ratios.

The current theoretical research on the axial compressive stability of FRP is mainly based on Euler's formula and Perry's theory, which are improved for the characteristics of different FRP materials, thus establishing the axial compressive stability theory of FRP and predicting their ultimate bearing capacity. For example, Lining Ding et al. (2018) [30] conducted axial compression tests on BFRP pipes with aspect ratios ranging from 6 to 90. Based on the experimental results, a stability equation was derived and verified for predicting the compressive strength of slender BFRP pipes using the Euler formula. Yang Zhan et al. (2018) [31] developed a new closed-form equation to determine the reduction factor of the overall flexural buckling of PFRP members under axial compression, based on the well-known Ayrton–Perry formula and the initial deflection of PFRP columns tested by other researchers. Li Chen et al. (2021) [32] used the Perry–Robertson formula based on the edge-failure criterion as the basic formula for calculating the overall stability coefficient of sandwich pipes. Then, based on experimental results, they derived the formula parameters and developed a calculation formula for the overall stability coefficient of FRP–foam sandwich pipes. They also improved the Euler formula to obtain a formula suitable for predicting the axial compressive strength of FRP–foam sandwich pipes. Although these scholars have predicted the ultimate bearing capacity of FRP pipes under axial compression using classical theories and established stability coefficient calculation equations for different FRP materials, only a few studies have predicted the axial compression behaviour of FRP columns used in large-span spatial structures.

To investigate the feasibility of using FRP tubes in large-span spatial structures, an axial compression test was conducted on FRP tubes with a slenderness ratio between 20 and 140. The test results provided valuable information on the compressive buckling behaviour of the tubes, specifically their overall stability, load-carrying capacity, and failure mode. To further enhance the understanding of the axial compressive behaviour of FRP tubes, two theoretical models were employed. The first model was the load-lateral deflection model for poly-ethylene terephthalate (PET) FRP-confined CFST columns (PFCCFSTs) [33], while the second model was the axial stress–strain model for double-skin tubular stub columns (DSTCs) [34]. By comparing the test results with the theoretical predictions, this study aims to demonstrate the potential of using high-performance composite FRP in large-span spatial structures and to promote the development of environmentally friendly and high-performance FRP materials in this field.

2. Materials and Methods

2.1. Materials

The BFRP tubes consisted of nanometre montmorillonite composite fibre material. BFRP tubes with nanometre montmorillonite modified biomass resin were selected as the matrix material and basalt fibre was the reinforcing material. The surface layer of the board had a silicon nitride coating, which enhanced its wear resistance, weather resistance, and self-cleaning property. Basalt fibre is a type of inorganic, environmentally friendly, high-performance fibre material fabricated using natural basalt ore, which is crushed and melted at 1500 °C, and brushed using a platinum–rhodium alloy leaky plate. Nanometre montmorillonite is a montmorillonite with a diameter of less than 100 nm, which is obtained from montmorillonite raw material through intercalation, modification, and stripping. The adsorption capacity of the product is enhanced by up to three times compared to that of conventional montmorillonite-based materials. Silicon nitride, a superhard compound composed of nitrogen and silicon, possesses several remarkable properties, including high temperature resistance, wear resistance, corrosion resistance, oxidation resistance, lubrication, and self-cleaning. Due to these properties, silicon nitride has found broad applications in the military industry. The abovementioned main raw materials were interspersed with the molecular chains of the polymer in the nanometre montmorillonite nanosheets through special processes, and connected them through polymer molecules in the form of chemical bonds. This produced nano-effects that significantly improved the properties of the materials, particularly the mechanical properties, heat resistance, and dimensional stability.

The density (ρ), Barcol hardness, fibre volume fraction, insoluble content of resin, water absorption, glass transition temperature (T_g), tensile strength (main fibre direction) (f_{tm}), tensile strength (secondary fibre direction) (f_{ts}), compressive strength (main fibre direction) (f_{cm}), compressive strength (secondary fibre direction) (f_{cs}), and shock resistance of the BFRP material are provided in Table 1 [35].

Table 1. Physical and mechanical properties of nanometre montmorillonite composite fibre material.

Performance	Performance Index
$\rho/(\text{kg}\cdot\text{m}^{-3})$	≤ 2000
Barcol hardness/(HBa)	≥ 50
Fibre volume fraction/%	≥ 70
Insoluble content of resin/%	≥ 90
Water absorption/%	≤ 1.0
$T_g/^\circ\text{C}$	≥ 200
f_{tm}/MPa	≥ 400
f_{ts}/MPa	≥ 10
f_{cm}/MPa	≥ 100
f_{cs}/MPa	≥ 15
Shock resistance/ $(\text{kJ}\cdot\text{m}^{-2})$	≥ 240

2.2. Specimens

2.2.1. Size of the Specimens

It is necessary to select the appropriate slenderness ratio to include the length of the rod with different failure modes (local failure, critical failure, and buckling failure). This study tested a total of 10 groups of FRP specimens with aspect ratios ranging from 20 to 140, with two specimens in each group.

According to the mechanics of materials, the slenderness ratio (λ), radius of gyration (i), effective length (l_0), and sectional inertia moment (I) can be expressed as follows:

$$\lambda = \frac{l_0}{i} \quad (1)$$

$$i = \sqrt{\frac{I}{A}} \quad (2)$$

$$l_0 = u_0 l \quad (3)$$

$$I = \frac{\pi(D^4 - d^4)}{64} \quad (4)$$

The following expression is obtained using Equations (1)–(4):

$$l = \frac{\lambda \sqrt{\frac{I}{A}}}{u_0} = \frac{\lambda \sqrt{\frac{\pi(D^4 - d^4)}{64A}}}{u_0} \quad (5)$$

where A , D , and d represent the cross-sectional area, and outer and inner diameters of BFRP tubes, respectively. u_0 denotes the coefficient for effective length of BFRP tubes, which was selected as 1.0 according to GB50017-2017 [34]. Circular BFRP tubes of eleven slenderness ratio gradients were selected for this study. The shape of the tubes is shown in Figure 1, and the slenderness ratio (λ), length (l), section outer diameter (D), section inner diameter (d), and thickness of the tube (t) are presented in Table 2. The length l is calculated using Equation (5).

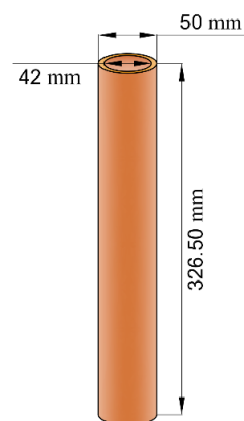


Figure 1. Test specimen Y-20-01.

Table 2. The dimensions of the test specimens.

Specimen Labels	λ	l (mm)	D (mm)	d (mm)	t (mm)	D/t Ratio
Y-20	20	326.4966	50	42	4	12.5
Y-40	40	652.9931	50	42	4	12.5
Y-60	60	979.4897	50	42	4	12.5
Y-80	80	1305.986	50	42	4	12.5
Y-90	90	1469.234	50	42	4	12.5
Y-100	100	1632.483	50	42	4	12.5
Y-110	110	1795.731	50	42	4	12.5
Y-120	120	1958.979	50	42	4	12.5
Y-130	130	2122.228	50	42	4	12.5
Y-140	140	2285.476	50	42	4	12.5

2.2.2. Mechanical Parameters of the BFRP Tubes

BFRP pipes are produced via the pultrusion moulding method, whereby a prepreg is applied onto a mould surface and subsequently solidified through a heating process. The prepreg is arranged in layers oriented at $[0^\circ/90^\circ]$ and comprises 60% fibre content. The BFRP samples used for material property testing were fabricated using identical layer angles, thickness, fibre content, and curing procedures as the aforementioned BFRP pipes. The material properties of the BFRP tubes, which were determined from the material property tests, are presented in Table 1.

2.3. Test Scheme

Figure 2 shows the experimental setup and instrumentation used for axial compression testing. The BFRP tube was circular and compressed using a hydraulic jack with a capacity of 500 kN (accuracy = 0.1 kN) and supported by a pair of parallel bi-directional limited-angle hinges. The top and bottom ends of the specimen were connected to the reaction frame and the jack, respectively. To measure the load applied to the specimen, a load sensor was installed between the jack at the bottom and the hinge support. Strain gauges were installed at the mid-span and 1/4 surface of the specimen, with four sets of strain gauges arranged equidistantly along the circumferential direction of the specimen as shown in Figure 3. Each set included a longitudinal strain gauge and a transverse strain gauge. Two orthogonal horizontal displacement transducers were used to measure the transverse deformation of the specimen at mid-span, with their measuring directions parallel and perpendicular to the predicted buckling plane, respectively. To measure the vertical displacement of the specimen ends, a vertical displacement transducer (model YHD-200; accuracy = 0.1 mm, sensitivity = 100 $\mu\epsilon$ /mm) was installed at the bottom of the specimen. When installed on the loading frame, a bubble level was used to ensure the straightness of the specimen. Under displacement control, a compression load was applied at a rate of 1 mm/min until failure occurred. The DH data acquisition system (model DH3816N) was used to collect data from the load sensor, strain gauges, and displacement transducers.

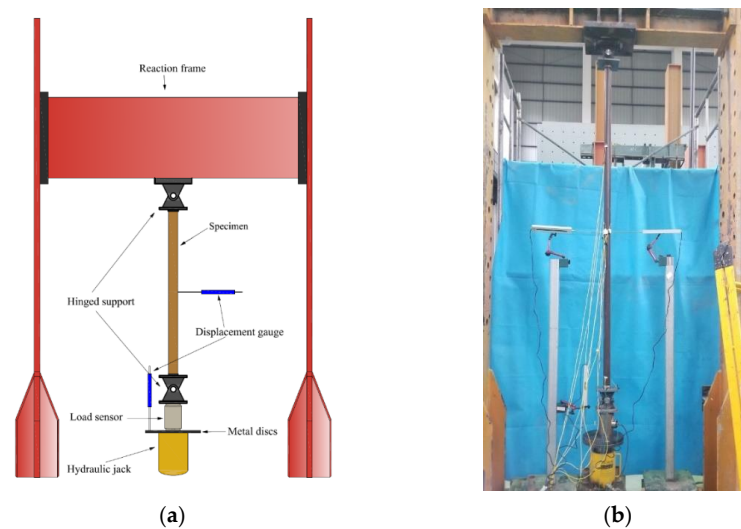


Figure 2. Test device and acquisition system. (a) Schematic of equipment. (b) Image of equipment.

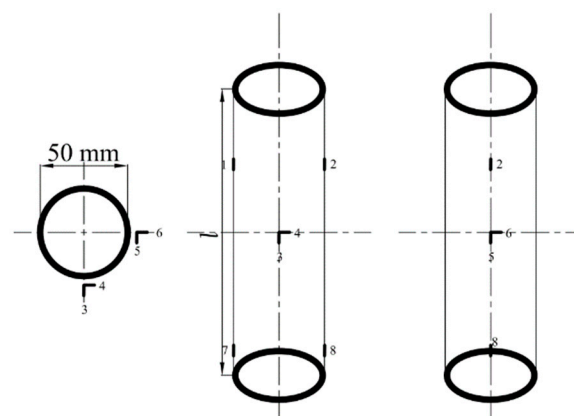


Figure 3. Arrangement of strainometers.

3. Experimental Results

3.1. Failure Modes of Unbuckling Specimens

The failure modes of unbuckling specimens are shown in Figure 4. The deflection of the upper support was observed under loading. The deflection of the upper support gradually increased with an increase in load. Finally, end failure was observed due to the overload, which was accompanied by a loud splitting sound. The enormous pressure caused severe damage to the end of the specimen, and cracks appeared in the tube wall (Figure 4).

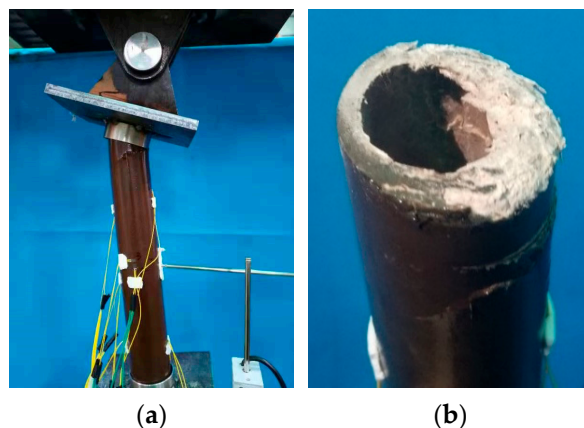


Figure 4. Load- and end-damage details of unbuckling specimens. (a) Loading. (b) End damage.

3.2. Failure Modes of Buckling Specimens

The failure modes observed in the buckling specimens were similar, as depicted in Figure 5. However, the deformation process differed from that of the unbuckling specimens. Upon loading, transverse deformation of the BFRP tube was observed, which increased slowly with the increase in the load. Once the transverse deformation reached 2–10 mm, the axial load remained relatively constant, while the transverse deformation rapidly developed. Ultimately, the specimen experienced buckling failure, which was accompanied by a loud splitting sound. The tensile side of the failed BFRP tube remained intact, while the compressive side exhibited buckling deformation, and cracks appeared on the tube wall, as shown in Figure 6. The failure location of BFRP tubes was approximately at the midpoint of the span. Multiple longitudinal cracks were observed on the specimen body. For instance, the longest crack on specimen Y-60-01 extended from the upper end to 63 mm (Figure 6). The remaining cracks were classified based on their length as 25, 18, 8, and 7.2 mm, with a few cracks ranging from 3 to 6 mm. One end of the specimen was damaged while the other end remained undamaged.



Figure 5. Deformation development of specimen Y-110-01.

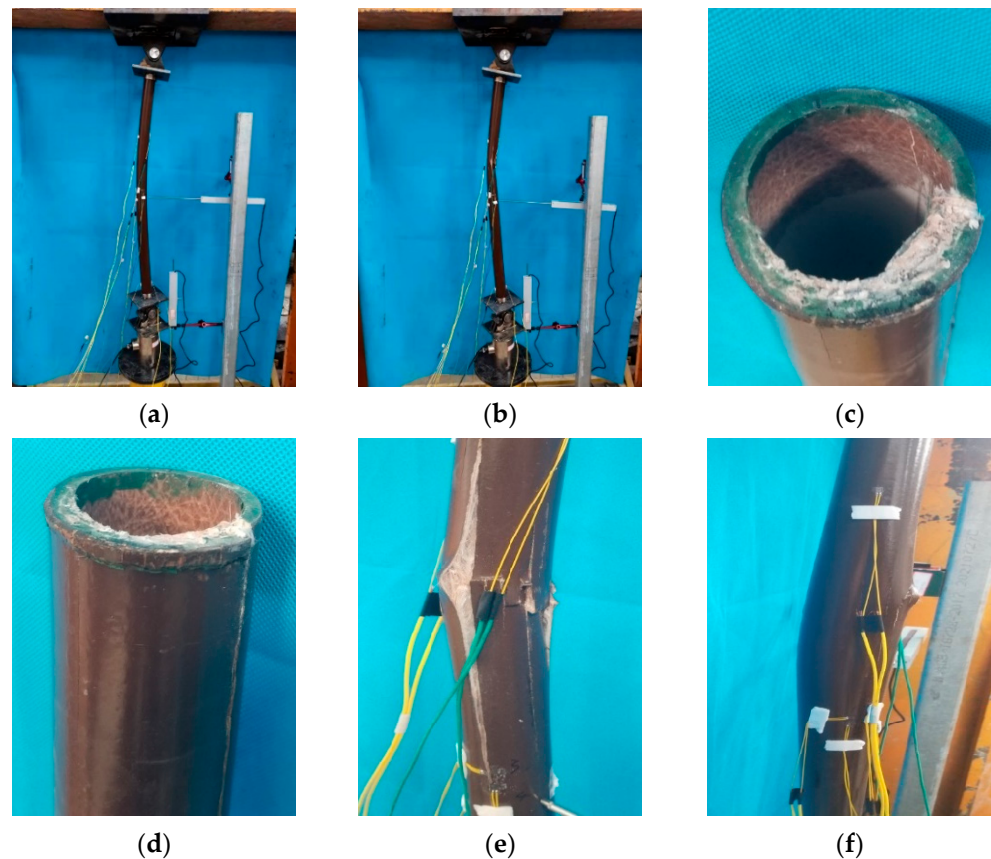


Figure 6. Loading- and end-damage details of buckling specimens. (a) Loading. (b) Mid-span damage. (c) End-damage front. (d) End-damage side. (e) Compression side. (f) Tension side.

3.3. Experimental Results

The following sections will report the experimental results concerning the critical buckling load and modes of failure. The critical buckling load is defined as the maximum load that a specimen can sustain before failure occurs. The axial compression test was conducted on two sets of BFRP tubes with slenderness ratios between 20 and 140. The test results of two sets of identical specimens showed slight differences, which may be attributed to different initial defects of BFRP tubes during manufacturing.

3.3.1. Critical Buckling Load

The critical buckling load (P_{max}), vertical displacement under critical buckling load (Δ_{pmax}), deflection at critical buckling load (y_{pmax}), and the ratio of the distance from the damaged location to the mid-span point and the total length of the specimen (α) are shown in Table 2. The P_{max} of specimens with a slenderness ratio in the range of 20–90 gradually decreased by approximately 10 kN when the slenderness ratio was increased by 20. The P_{max} of specimens with a slenderness ratio in the range of 90–140 gradually decreased by approximately 2–5 kN with an increase in the slenderness ratio by 10.

The value of α was irregular as observed from Table 3. The slight difference in stresses near the mid-span resulted in the observed phenomenon. The initial damage occurred at positions with severe initial defects. The initial transverse deformation of the BFRP tubes under load was attributed to the initial geometrical defects, including, but not limited to, initial eccentricity, micro-cracks, and uneven stiffness. The change in α indicated that the failure location of the specimen gradually shifted towards the mid-span with an increase in the slenderness ratio, but not strictly to the mid-span. This is because the stress difference at the mid-span is small, and the failure will occur first at the position with larger initial defects. The failure modes also followed this rule.

Table 3. P_{\max} , $\Delta_{p\max}$, $y_{p\max}$, and α of test specimens.

Specimens	P_{\max}/kN	$\Delta_{p\max}/\text{mm}$	$y_{p\max}/\text{mm}$	$\alpha/\%$
Y-20	70.75	2.86	—	47.70%
Y-40	62.00	7.76	—	15.63%
Y-60	51.25	4.40	14.10	10.42%
Y-80	39.75	6.96	22.62	2.30%
Y-90	26.75	3.84	4.72	0.68%
Y-100	21.00	12.01	80.32	4.29%
Y-110	23.75	20.30	120.34	1.67%
Y-120	18.25	22.62	140.89	9.09%
Y-130	15.75	2.75	29.99	0.94%
Y-140	13.25	2.57	29.46	12.5%

3.3.2. Failure Modes

The failure modes of the BFRP tubes are shown in Table 4. These failure modes include three modes, local failure, critical failure, and buckling failure. Local failure was characterized when buckling did not occur and the end was severely damaged (Figure 4). Critical failure refers to buckling and slight end damage or cracking (Figure 5). Buckling failure refers to buckling and an intact end (Figure 6). This was observed because the critical buckling load of the specimens was large when the slenderness ratio was considerably small. The specimens did not buckle with an increase in load, and the stress at the end exceeded the limit of the end or the limit of the material. Therefore, the end was severely damaged. The critical buckling load decreased as the slenderness ratio of the specimen increased, with the relationship being inversely proportional to the square of the ratio. The bearing capacity remained unchanged when the load reached or approached the critical buckling load, and the specimen exhibited buckling and the lateral displacement gradually increased. Subsequently, the end stress decreased accordingly. Therefore, the end was slightly damaged or cracked. The critical buckling load of the specimen decreased as the slenderness ratio increased. The stress at the end was lower than that of the ultimate stress when the applied load was close to the critical buckling load. Therefore, the end was not damaged.

Table 4. The failure modes of test specimens.

Slenderness Ratio	Whether It Is Buckling or Not	End Damage	Failure Modes
20	No	Severe damage	Local failure
40	Yes	Slight damage	Critical failure
60	Yes	Slight damage	Critical failure
80	Yes	Crack	Critical failure
90	Yes	Intact	Buckling failure
100	Yes	Intact	Buckling failure
110	Yes	Intact	Buckling failure
120	Yes	Intact	Buckling failure
130	Yes	Intact	Buckling failure
140	Yes	Intact	Buckling failure

According to the abovementioned description, the damaged area at the end of the specimen gradually decreased as the slenderness ratio increased until it was completely undamaged (Figures 7 and 8). Change in damage area/section area (Figures 7 and 8 and Table 5) reflects the damage of the specimen end when different slenderness ratio specimens reached or approached the critical load under axial compression. This is a potential engineering application, and can be used to optimize the end section and select the appropriate end reinforcement for different slenderness-ratio specimens according to specific engineering applications.

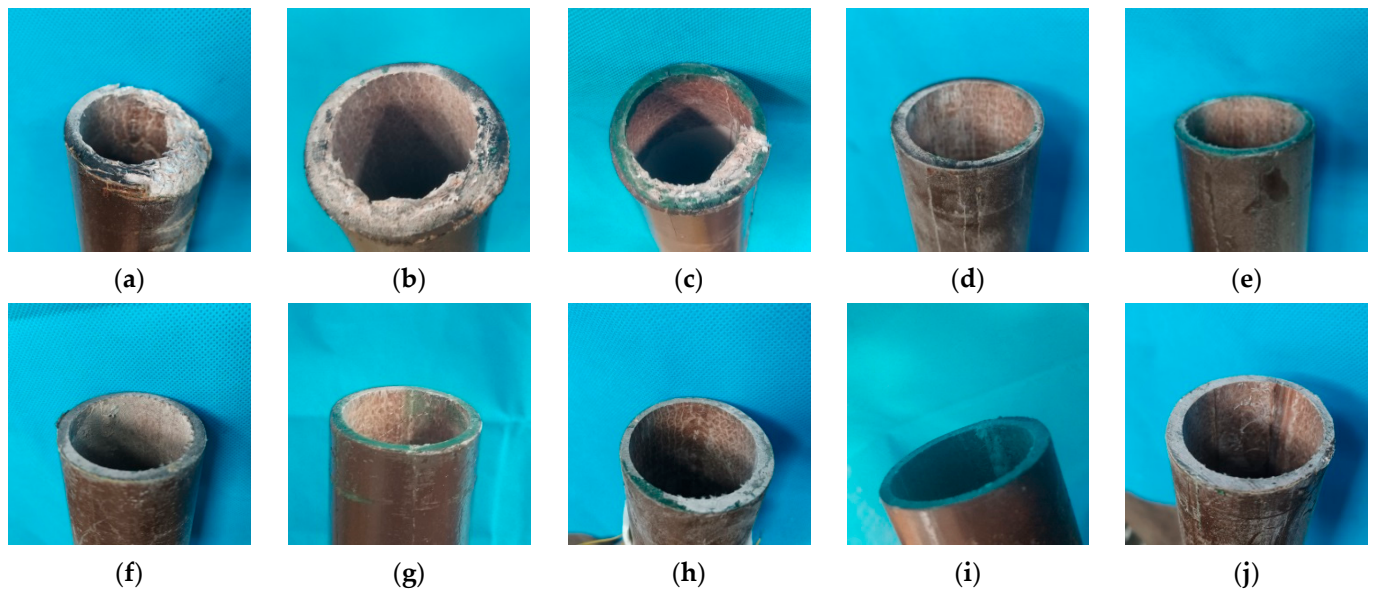


Figure 7. End damage of each test specimen. (a) Y-20. (b) Y-40. (c) Y-60. (d) Y-80. (e) Y-90. (f) Y-100. (g) Y-110. (h) Y-120. (i) Y-130. (j) Y-140.

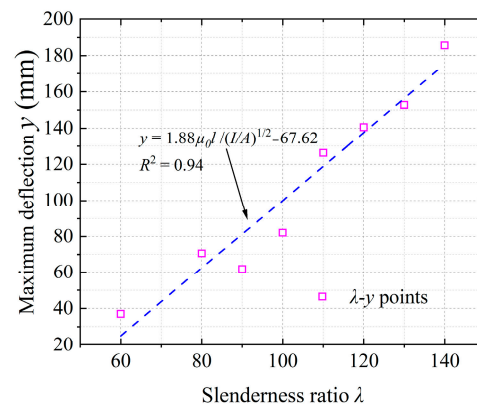


Figure 8. Regression analysis of maximum deflection.

Table 5. The cross-sectional damage area of test specimens.

Slenderness Ratio (λ)	20	40	60	80	90	100	110	120	130	140
End damage area (mm ²)	491.85	373.75	303.01	3	0	0	0	0	0	0
Damage area/section area (%)	85.13%	64.69%	52.45%	0.52%	0%	0%	0%	0%	0%	0%

Notes: Damage area/section area (%) is obtained by measuring the circumference of the damaged end of the specimen with a calliper and dividing it by the total circumference.

4. Analysis of Test Results

4.1. Vertical Displacement–Lateral Deflection Behaviour

The maximum deflection/length (l) increased as the slenderness ratio increased (Table 6). This indicated that the degree of overall instability of the BFRP tubes increased as the slenderness ratio increased. Figure 8 depicts the fitted line between slenderness ratio (λ) and maximum deflection. The following expressions were obtained using Equations (1)–(3) and regression analysis (Figure 8) of the experimental results of BFRP tube:

$$\lambda = \mu_0 l / \sqrt{\frac{I}{A}} \quad (6)$$

$$y = 1.88\mu_0 l / (I/A)^{1/2} - 67.62 \quad (7)$$

Table 6. The maximum deflection of test specimens.

Slenderness Ratio (λ)	60	80	90	100	110	120	130	140
Maximum deflection (mm)	37.06	70.50	61.80	82.08	126.25	140.55	152.76	185.66
Maximum deflection/ l (%)	3.84	5.40	4.21	5.03	7.03	7.18	7.20	8.12
Δ -start buckling (mm)	2.12	2.25	3.02	2.54	2.50	2.81	2.49	2.52

The data points were distributed around the line $y = 1.88x - 67.62$. The regression coefficient was $R^2 = 0.94$. It is evident that the data points were significantly close to the fitted line, which reflected the success of the experiment, small data dispersion, and effectiveness of the data.

The deflection did not change significantly at the early stage of loading, as shown in Figure 9. The deflection significantly increased when the vertical displacement was about 2.5 mm, and the rate of increase gradually slowed down thereafter. This indicated that the buckling specimens exhibited instability when the axial displacement was approximately 2.5 mm. However, the specimen did not fracture. Additionally, it indicated that BFRP tube had optimum toughness, and the circular cylindrical member exhibited buckling at an axial displacement of approximately 2.5 mm regardless of the slenderness ratio (Table 6), which can be used for engineering applications. 2.5 mm is suitable for the configurations considered in this study. The influence of the geometric shape remains to be further investigated.

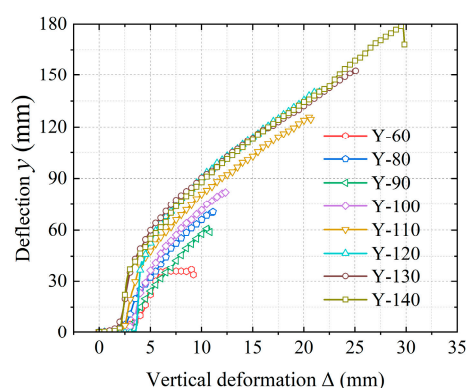


Figure 9. Deflection- Δ curves.

4.2. Load-Lateral Displacement Behaviour

The load-lateral deflection curves are shown in Figure 10. Lateral deflection refers to the deflection at the midpoint of the specimen when it is loaded. The load-lateral deflection curves of different failure modes exhibited a few differences. The curve of critical failure mode (Figure 10a) had a slower rate of load rise in the initial elastic range and a shorter stabilization plateau after reaching critical load. The slower rate of load rise was due to the faster deflection of the hinge support with an increase in load. This was observed because the faster deflection of the hinge support increased the lateral deflection, which decreased the rate of increase in load as shown in Figure 10a. The curve of buckling failure mode exhibited a rapid, approximately vertical rate of load rise in the initial elastic range and a long stable plateau after reaching the critical load. The rapid, almost vertical rate of load rise indicated that a significant deflection of the hinge support did not occur and the specimen did not exhibit buckling before the load reached or approached critical load. The load remained constant or slightly decreased after reaching the critical load, and finally stabilized until the maximum deflection was achieved (Figure 10b–h).

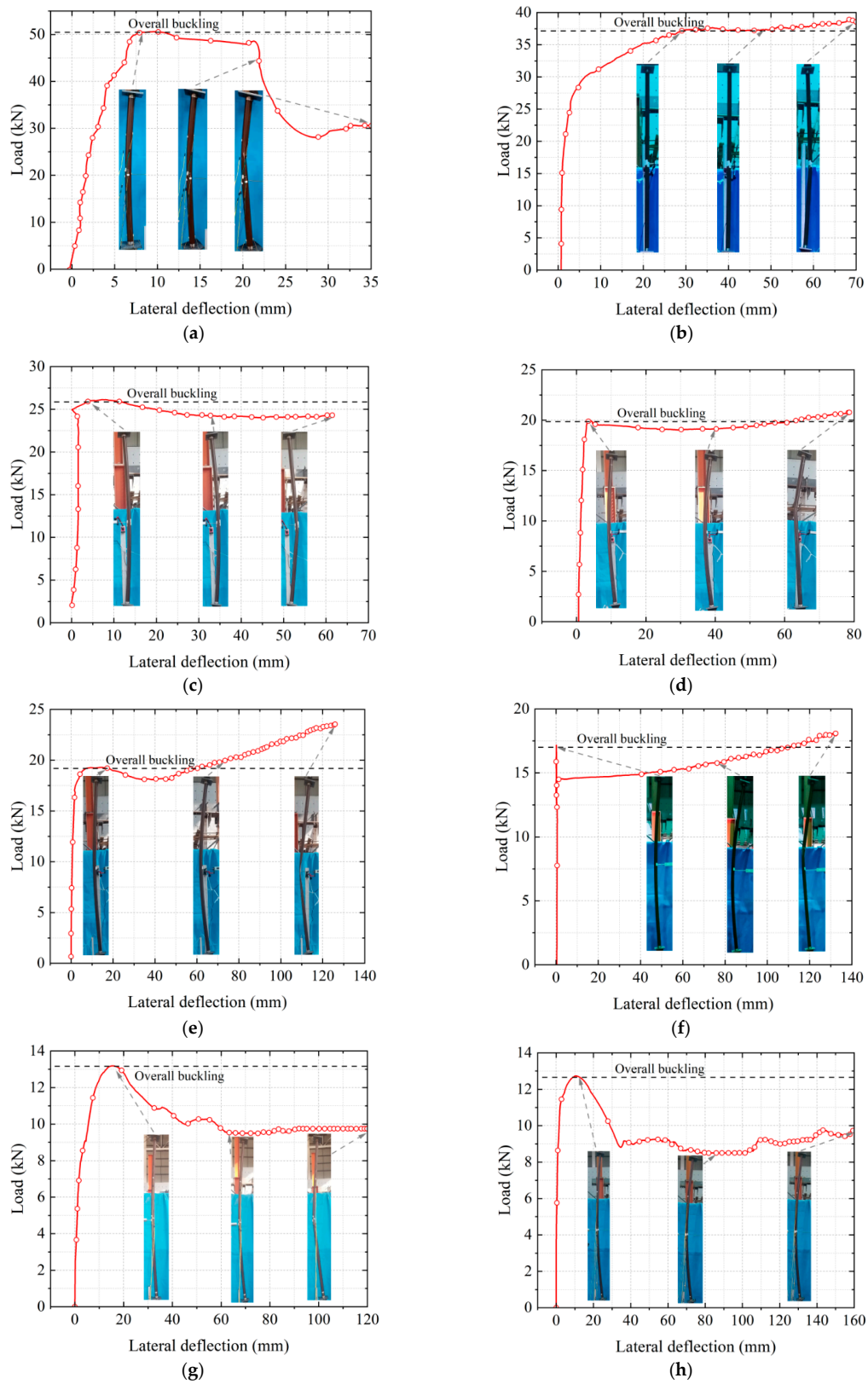


Figure 10. Load-lateral deflection curves. (a) $\lambda = 60$ -circular cross-section. (b) $\lambda = 80$ -circular cross-section. (c) $\lambda = 90$ -circular cross-section. (d) $\lambda = 100$ -circular cross-section. (e) $\lambda = 110$ -circular cross-section. (f) $\lambda = 120$ -circular cross-section. (g) $\lambda = 130$ -circular cross-section. (h) $\lambda = 140$ -circular cross-section.

The specimens demonstrated comparable rates of load increase during the initial elastic range; however, they exhibited distinct ultimate (peak) loads (as shown in Figure 10) under varying slenderness ratios. This can be attributed to the differences among the specimens consisting of the same material but with different slenderness ratios. The peak loads showed an approximate difference of 10 kN when the slenderness ratio increased by 20. Moreover, as the slenderness ratio increased, the rate of load decrease decreased, indicating a smaller second-order effect after the peak loads.

4.3. Stress and Strain

4.3.1. Ultimate Bearing Capacity

The experimental results presented in Table 3 demonstrate that the critical buckling load (P_{\max}) of the BFRP tubes decreased as the slenderness ratio increased. This suggests that the overall instability of the specimens increased while their bearing capacity decreased as the slenderness ratio increased. The fitted line between the slenderness ratio (λ) and ultimate bearing capacity is illustrated in Figure 11. According to Figure 11, it can be seen that when the member is in the linear elastic range, the ultimate load is inversely proportional to the square of the slenderness ratio. Beyond the linear elastic range, the ultimate load does not increase sharply with the increase in the slenderness ratio. The response of the ultimate-load–slenderness ratio presents a double curvature, which is also in accordance with the theory. Regression analysis of the experimental results of BFRP tubes produced the following expressions:

$$y = -4.17 \times 10^{-7} \lambda^4 + 2.05 \times 10^{-4} \lambda^3 - 0.03 \lambda^2 + 1.1 \lambda + 55.69 \quad 25 \leq \lambda \leq 130 \quad (8)$$

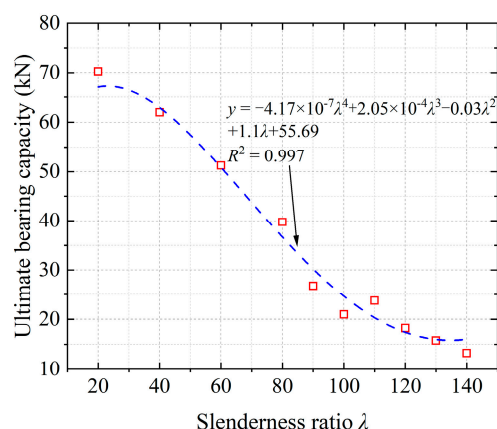


Figure 11. Regression analysis of ultimate bearing capacity.

It is evident that the data points were significantly close to fitted line. The coefficient of determination, R^2 , value of the fitted curve was 0.997, which indicated an optimal fit. Hence, the experiment had a small data dispersion, and the effectiveness of the data was verified.

4.3.2. Stress–Strain Relationship

Figures 12 and 13 illustrate the stress–strain curves of the BFRP tubes. The stresses depicted in the figures represent the average strain throughout the entire length of the member. Prior to reaching the ultimate compressive strength, the axial strain of both unbuckled and buckled specimens displayed a linear response to axial stress. For unbuckled specimens, damage or cracking occurred at the end of the BFRP tubes once the ultimate compressive strength was reached, and the curve trend exhibited no regularity. In the case of buckled specimens, rapid buckling occurred as the axial stress reached the ultimate compressive strength, with the axial stress maintained at roughly 75–90% of this value. These buckled specimens showed optimal ductility, although a few of the curves exhibited a considerable decrease after reaching the axial ultimate compressive strength

due to hinge-support deflection (as shown in Figures 12 and 13). Subsequently, the curves for buckling specimens exhibited a yielding stage, whereas the corresponding curve for unbuckling specimens did not demonstrate a distinct yield stage. Figure 13 displays the stress–strain curves of BFRP tubes, which can be divided into three distinct stages using three characteristic points denoted as A, B, and C. The three distinct stages are shown as follows:

- (1) Elastic stage (OA): Prior to the stress reaching the axial ultimate compressive strength, the BFRP tubes are in the elastic stage. During this stage, the stress–strain curve exhibits a linear increase. The specimens yield at point A, marking the end of the elastic stage.
- (2) Elastic–plastic stage (AB): The stress decreases at point A, but briefly. Simultaneously, buckling of the specimens is observed.
- (3) Plastic stage (BC): Specimens at this stage exhibit stable bearing capacity in this stage, and the deflection rapidly increases. The specimens in this stage of unloading restore their original approximate shape. However, their bearing capacity is decreased. This indicates that the specimens have optimum elastic–plastic performance.

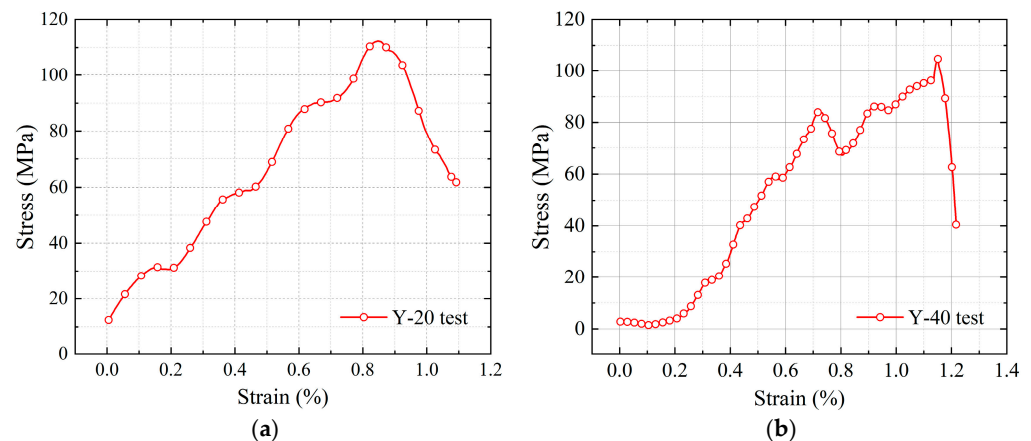


Figure 12. Stress–strain curve of unbuckling specimens. (a) $\lambda = 20$ -circular cross-section. (b) $\lambda = 40$ -circular cross-section.

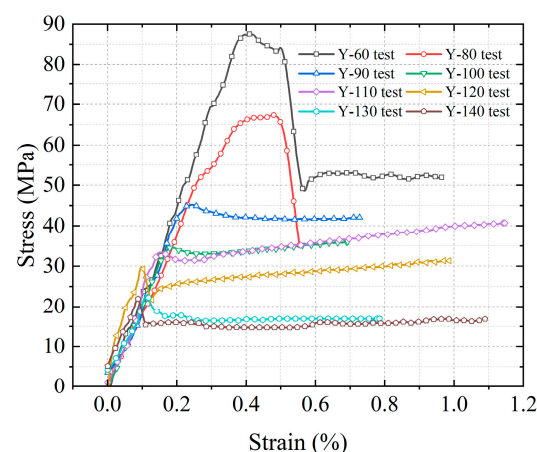


Figure 13. Stress–strain curve of buckling specimen.

5. Models

To analyse the behaviour of the BFRP tube under axial compression, a theoretical analysis was conducted using two existing models. The first model was the load-lateral deflection model for poly-ethylene terephthalate (PET) FRP-confined CFST columns (PFC-CFSTs) [33], while the second model was the stress–strain model of the double-skin tubular

stub columns (DSTCs) [34]. However, it was observed that neither of these two models was fully adequate for simulating the axial compression behaviour of the BFRP tube. Therefore, a comparison was made between the predictions of these models and the experimental results presented in this section to identify the differences and improve the models. This comparison could serve as a basis for developing a more appropriate and precise analytical model for simulating the behaviour of BFRP tubes under axial compression.

5.1. Load-Lateral Deflection Model

The behaviour of BFRP tubes under axial compression is characterized by post-buckling persistence, which is a critical feature that cannot be ignored. To address this, a three-stage load-lateral deflection model was proposed and depicted in Figure 14. The model comprises three distinct parts. Firstly, the linear portion (OA), which is an ascending straight line that extends from the origin point O ($\sigma_c = 0, \varepsilon_c = 0$) to point A ($\sigma_c = f_0, \varepsilon_c = \varepsilon_0$). Secondly, the quadratic parabola (AB), which is an ascending curve that extends from point A to the transition point B ($\sigma_c = f_t, \varepsilon_c = \varepsilon_t$). Lastly, the linear portion (BC) is a gradually ascending straight line that begins at the transition point B and extends to the ultimate point C ($\sigma_c = f_{cu}, \varepsilon_c = \varepsilon_{cu}$). The proposed model takes into account the post-buckling persistence of BFRP tubes, which is crucial in accurately predicting their behaviour under axial compression.

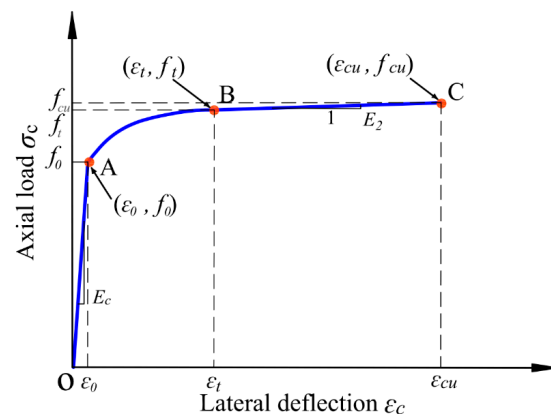


Figure 14. Three-stage load-lateral deflection model of fibre reinforced composites.

The second part of the stress–strain model can be expressed as a quadratic parabola, which can be derived mathematically using the coordinates of point A and transition point B, and the initial slope E_{sec} , as described by Equation (10), which is similar to that of the model proposed by Zeng [33] for poly-ethylene terephthalate (PET) FRP-confined CFST columns (PFCCFSTs).

Figure 15 compares the predicted load-lateral deflection behaviour of BFRP tubes with the actual experimental results. The model's predicted results are in good agreement with the experimental data, indicating that the model can accurately predict the axial compression behavior of BFRP tubes.

$$\sigma_c = E_c \varepsilon_c \quad 0 \leq \varepsilon_c \leq \varepsilon_0 \quad (9)$$

$$\sigma_c = f_0 + E_c(\varepsilon_c - \varepsilon_0) + a(\varepsilon_c - \varepsilon_0)^n \quad \varepsilon_0 \leq \varepsilon_c \leq \varepsilon_t \quad (10)$$

$$\sigma_c = f_t + E_2(\varepsilon_c - \varepsilon_t) \quad \varepsilon_t \leq \varepsilon_c \leq \varepsilon_{cu} \quad (11)$$

where (ε_0, f_0) is the termination point, (ε_t, f_t) is the transition point, and $(\varepsilon_{cu}, f_{cu})$ is the ultimate point. The parameters described in Equations (9) and (10) can be determined in the following equations:

$$n = \frac{E_2 - E_c}{E_{sec} - E_c} \quad (12)$$

$$E_2 = \frac{f_{cc} - f_t}{\varepsilon_{cu} - \varepsilon_t} \quad (13)$$

$$E_{sec} = \frac{f_t - f_0}{\varepsilon_t - \varepsilon_0} \quad (14)$$

$$a = \frac{E_{sec} - E_c}{(\varepsilon_t - \varepsilon_0)^{(n-1)}} \quad (15)$$

$$f_0 = b_1\alpha + b_2\alpha^2 + B \quad (16)$$

$$f_t = f_0 + E_c(\varepsilon_t - \varepsilon_0) + a(\varepsilon_t - \varepsilon_0)^n \quad (17)$$

$$\alpha = \frac{\lambda - 40}{20} \quad (18)$$

The calculation coefficients in the equation and results are listed in Table 7.

Table 7. The calculation coefficients of Equations (12)–(18).

E_c	E_{sec}	E_2	b_1	b_2	B	n	a
9.6588	0.2960	0.0220	−11.7299	0.8784	45.7105	1.0293	−8.5501

5.2. Stress–Strain Model

The stress–strain curves show that post-peak softening is an important and unignorable compressive feature of BFRP tubes. Therefore, to account for this behaviour, a stress–strain model was proposed, as shown in Figure 16. This model consists of three segments. The first segment is the ascending quadratic parabola (OA), which extends from the origin point O ($\sigma_c = 0, \varepsilon_c = 0$) to the peak point A ($\sigma_c = f'_p, \varepsilon_c = \varepsilon_p$). The second segment is the descending linear line (AB), which stretches from the peak point A to the transition point B ($\sigma_c = f'_t, \varepsilon_c = \varepsilon_t$). The third segment is the ascending linear line (BC), which starts at the transition point B and extends to the ultimate point C ($\sigma_c = f'_{cc}, \varepsilon_c = \varepsilon_{cu}$).

To obtain the equation for the quadratic parabola in the first part of the proposed stress–strain model, mathematical derivation can be performed using the coordinates of the original point O and peak point A, as well as the initial slope E_c . This derivation leads to the equation described by Equation (19), which was similar to that of the model proposed by Wang [34] for double-skin tubular stub columns (DSTCs).

$$\sigma_c = E_c\varepsilon_c + \frac{f'_p - E_c\varepsilon_p}{\varepsilon_p^2} \varepsilon_c^2 \quad 0 \leq \varepsilon_c \leq \varepsilon_p \quad (19)$$

$$\sigma_c = f'_p + E_1(\varepsilon_c - \varepsilon_p) \quad \varepsilon_p \leq \varepsilon_c \leq \varepsilon_t \quad (20)$$

$$\sigma_c = f'_t + E_2(\varepsilon_c - \varepsilon_t) \quad \varepsilon_t \leq \varepsilon_c \leq \varepsilon_{cu} \quad (21)$$

where E_c denotes the slope of OA. E_1 and E_2 denote the slopes of AB and BC, respectively, which are calculated as:

$$E_1 = \frac{f'_t - f'_p}{\varepsilon_t - \varepsilon_p} \quad (22)$$

$$E_2 = \frac{f'_{cc} - f'_t}{\varepsilon_{cu} - \varepsilon_t} \quad (23)$$

It is evident that the axial stresses and axial strains at the three key points (i.e., the peak point, transition point, and ultimate point) should be determined to obtain the entire three-stage stress–strain curve. $\varepsilon_p, \varepsilon_t, f'_p$ and f'_t are calculated using

$$\varepsilon_p = a_1\alpha + a_2\alpha^2 + A \quad (24)$$

$$\varepsilon_t = b_1\alpha + b_2\alpha^2 + B \tag{25}$$

$$f'_p = c_1\alpha + c_2\alpha^2 + C \tag{26}$$

$$f'_t = d_1\alpha + D \tag{27}$$

$$\alpha = \frac{\lambda - 40}{20} \tag{28}$$

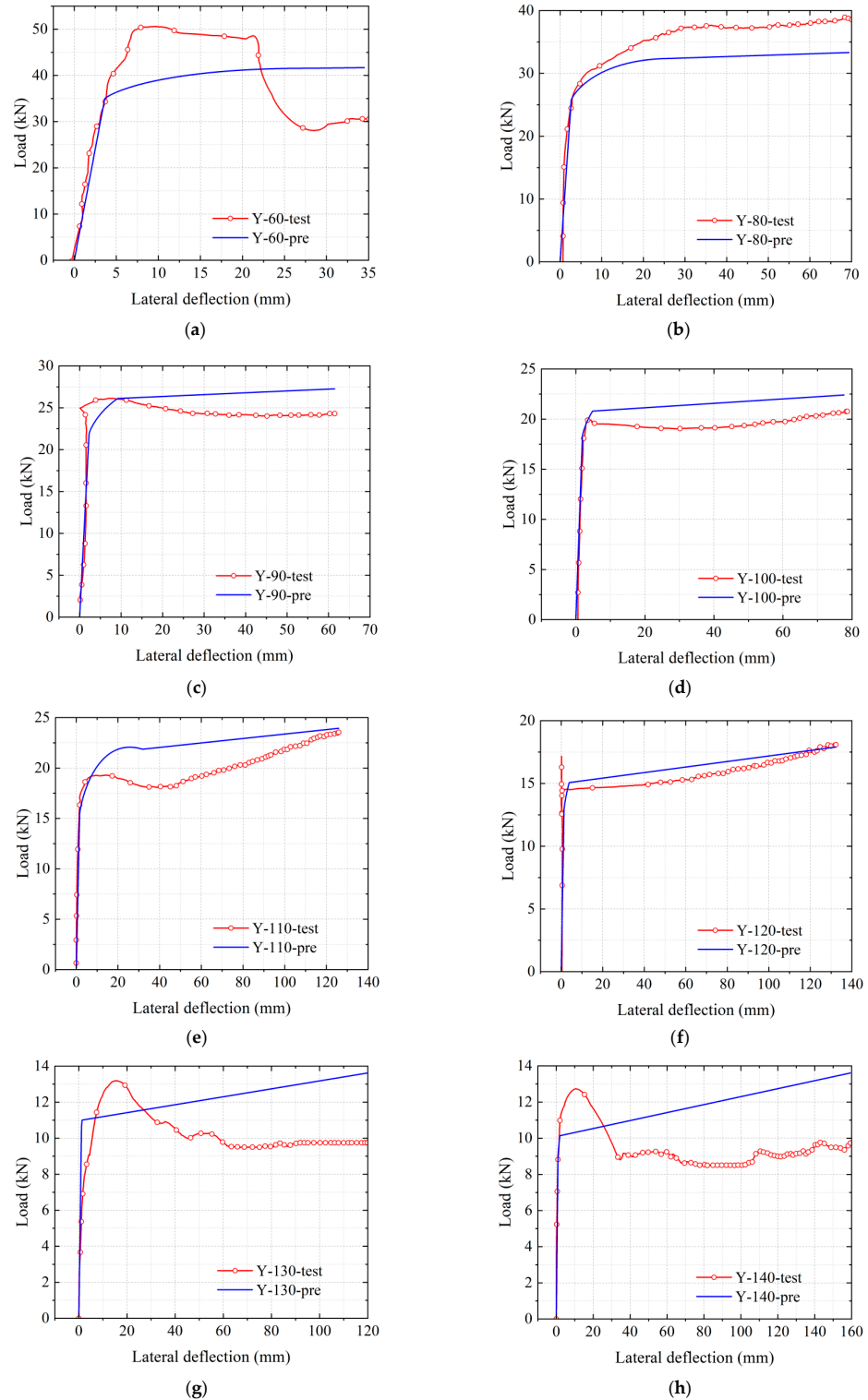


Figure 15. Cont.

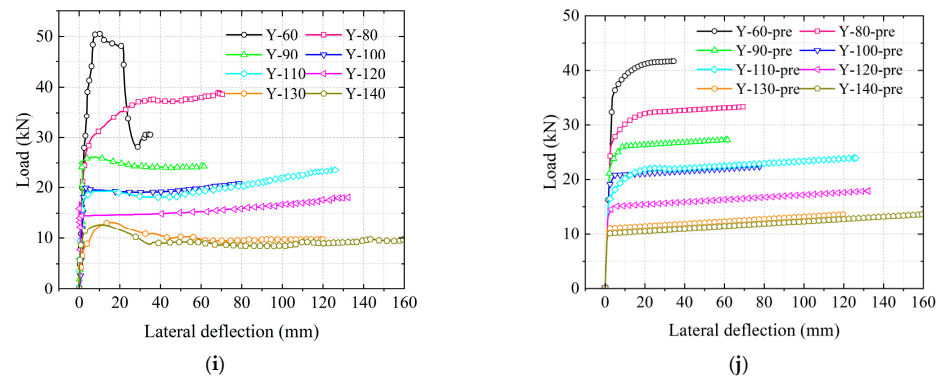


Figure 15. Comparison between the predictions of the proposed model and test results. (a) $\lambda = 60$ -circular cross-section. (b) $\lambda = 80$ -circular cross-section. (c) $\lambda = 90$ -circular cross-section. (d) $\lambda = 100$ -circular cross-section. (e) $\lambda = 110$ -circular cross-section. (f) $\lambda = 120$ -circular cross-section. (g) $\lambda = 130$ -circular cross-section. (h) $\lambda = 140$ -circular cross-section. (i) Test. (j) Prediction.

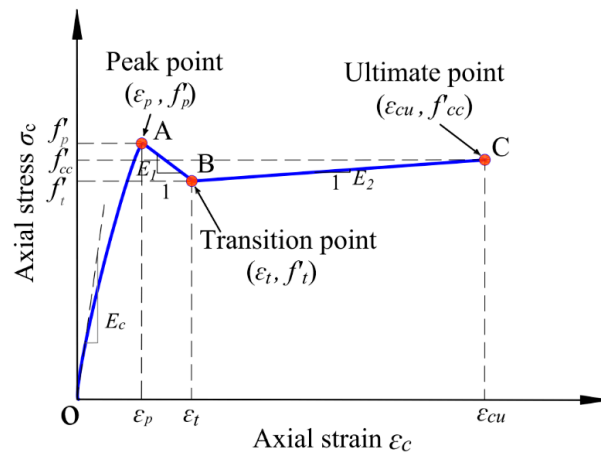


Figure 16. Three-stage stress–strain model of fibre reinforced composites.

The calculation coefficients in the equation and calculated results are provided in Tables 8 and 9.

Table 8. The calculation coefficients of Equations (24)–(27).

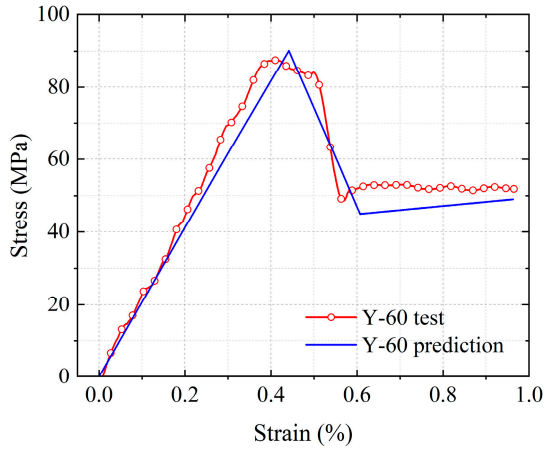
a_1	a_2	A	b_1	b_2	B	c_1	c_2	C	d_1	D
−0.1582	0.0109	0.5887	−0.2178	0.0150	0.8100	−40.8365	3.9641	126.9711	−8.7223	58.8179

Table 9. Results calculated using Equations (24)–(27).

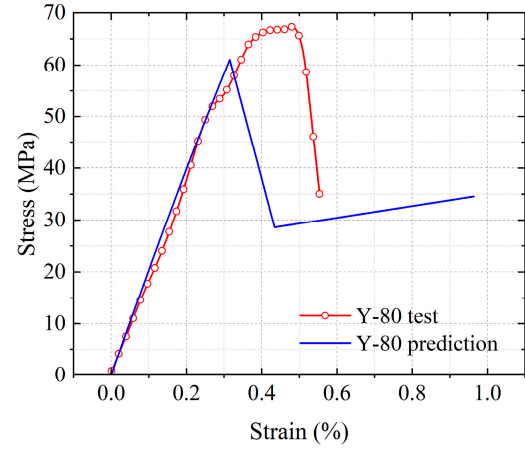
Specimens	E_c	E_1	E_2	ϵ_p	ϵ_t	f'_p	f'_t
Y-60	208.0713	−272.5178	11.2953	0.4414	0.6072	90.0987	50.0956
Y-80				0.3158	0.4344	61.1546	41.3733
Y-90				0.2611	0.3592	49.6556	37.0122
Y-100		−23.1684	5.7914	0.2118	0.2915	40.1386	32.6510
Y-110				0.1680	0.23127	32.6038	28.2899
Y-120		−226.9290	3.6775	0.1296	0.1785	27.0509	23.9287
Y-130				0.0966	0.1333	23.4802	19.5676
Y-140				0.0691	0.0956	21.8915	15.2064

Notes: E_c (208.0713) is suitable for slenderness ratios ranging from 60 to 140. E_1 (−272.5178) and E_2 (11.2953) are suitable for slenderness ratios ranging from 60 to 90. E_1 (−23.1684) and E_2 (5.7914) are suitable for slenderness ratios ranging from 90 to 110. E_1 (−226.9290) and E_2 (3.6775) are suitable for slenderness ratios ranging from 120 to 140.

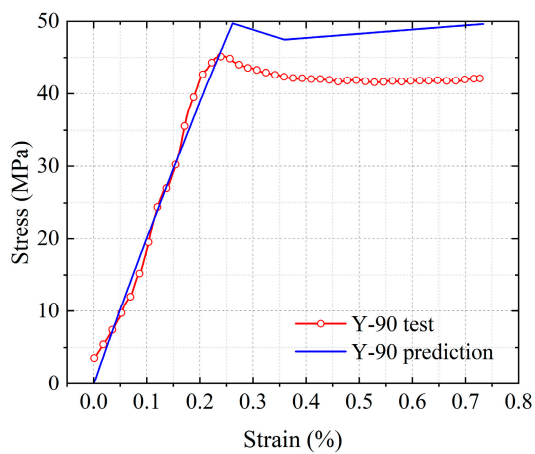
Figure 17 compares the predicted stress–strain behaviour of BFRP tubes with the actual experimental results. The model's predictions were found to be in good agreement with the experimental data, indicating that the model accurately predicts the mechanical behaviour of BFRP tubes.



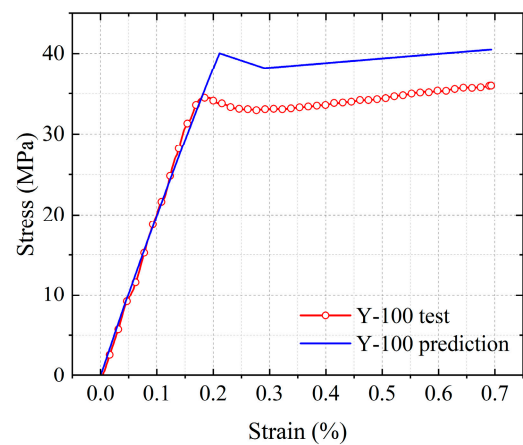
(a)



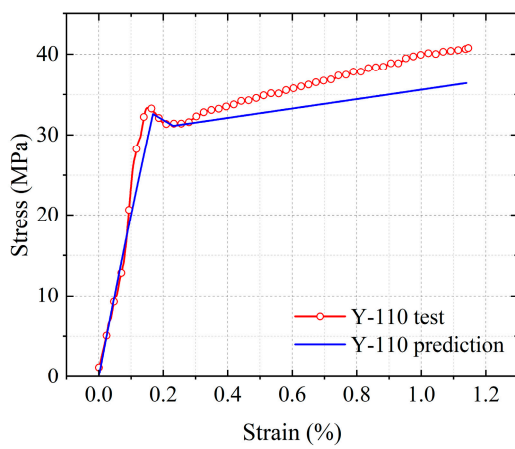
(b)



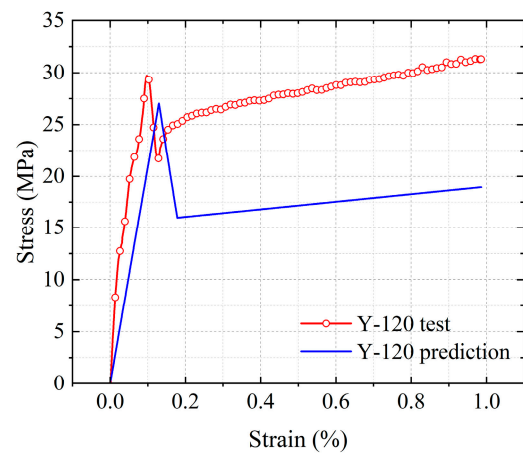
(c)



(d)



(e)



(f)

Figure 17. Cont.

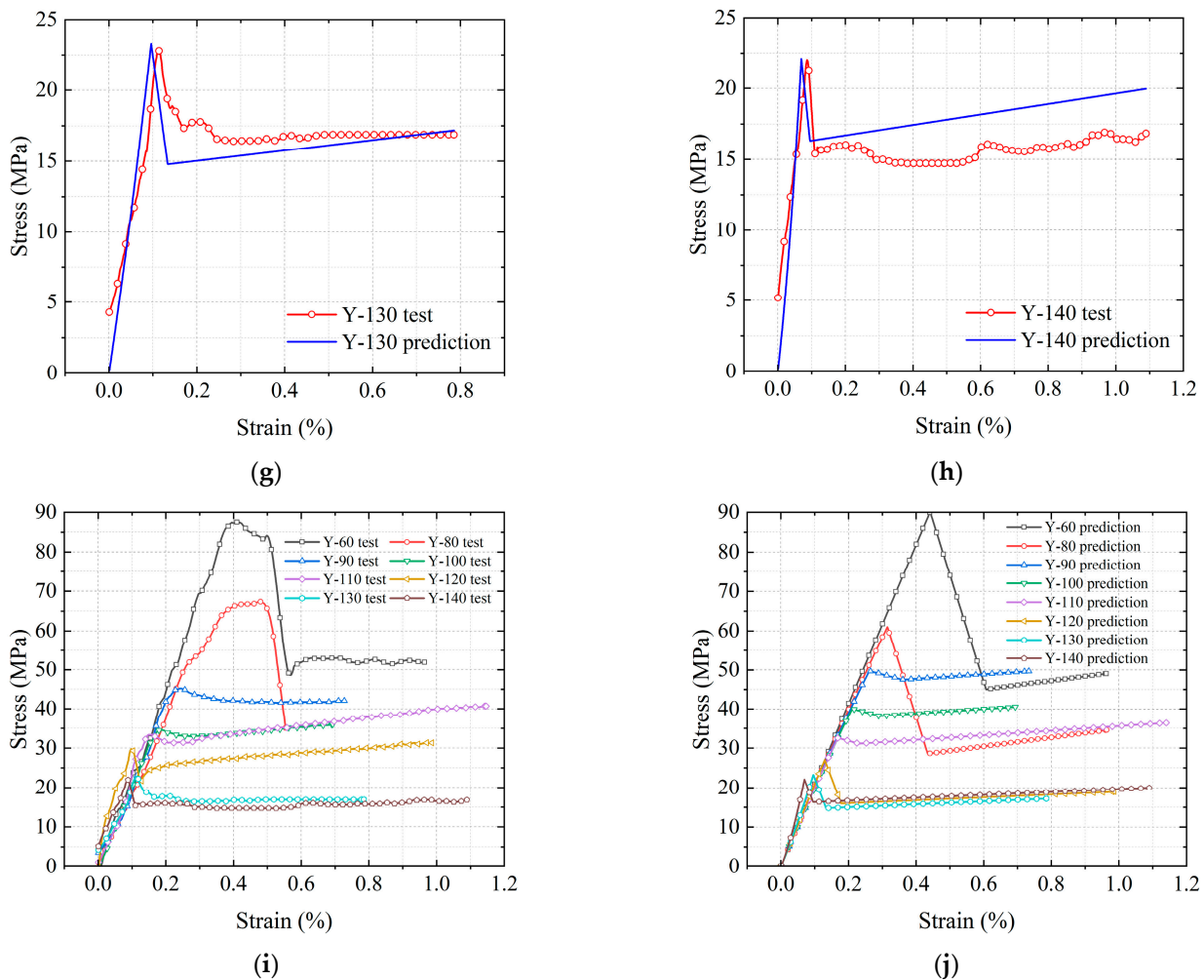


Figure 17. Comparison between the predictions of proposed model and the test results. (a) $\lambda = 60$ -circular cross-section. (b) $\lambda = 80$ -circular cross-section. (c) $\lambda = 90$ -circular cross-section. (d) $\lambda = 100$ -circular cross-section. (e) $\lambda = 110$ -circular cross-section. (f) $\lambda = 120$ -circular cross-section. (g) $\lambda = 130$ -circular cross-section. (h) $\lambda = 140$ -circular cross-section. (i) Test. (j) Prediction.

6. Conclusions

An experimental study was performed to study the mechanical performance of BFRP tubes under axial compression. The following conclusions were obtained through experimental investigation and analysis of test results:

- (1) The axial compression test conducted on slender BFRP tubes revealed three failure modes: local failure, critical failure, and buckling failure. Overall, buckling was identified as the primary failure mode under compression.
- (2) In the initial loading phase, there was little change observed in the deflection of the BFRP tubes. However, once the vertical displacement reached approximately 2.5 mm, the deflection increased significantly and continued to do so until failure. This abrupt instability in buckling specimens indicated a critical point of failure.
- (3) The BFRP tubes had similar load-ascending rates in the initial elastic range but different ultimate loads under varying slenderness ratios. Moreover, the load descending rate decreased as the slenderness ratio increased, suggesting a smaller second-order effect after the peak loads.
- (4) The typical stress–strain curves of BFRP tubes were divided into three parts: elastic stage (OA), elastic–plastic stage (AB), and plastic stage (BC).

- (5) The test stress–strain curves of the BFRP tubes closely matched the predicted curves (Y. L. Wang model [34]) in all three stages. The experimental load-lateral deflection behaviour of the BFRP tubes exhibited good consistency with the predicted models (J. J. Zeng model [33]) within the elastic stage, despite the ultimate loads being overestimated.

Author Contributions: Conceptualization, Methodology, Investigation, Writing—reviewing & editing, C.Z.; Investigation, Data curation, Writing—Data curation, Original draft preparation, Y.C.; Investigation, M.D. All authors have read and agreed to the published version of the manuscript.

Funding: This research was funded by the National Natural Science Foundation of China (Grant No. 51868013, 51508482), Natural Science Foundation of Tibet Autonomous (Grant No. XZ202102YD0035C), and Sichuan Science and Technology Program (Grant No. 2020JDTD0021).

Data Availability Statement: The data presented in this study are available on request from the corresponding author. The data are not publicly available due to [Fund Requirements].

Acknowledgments: The authors are grateful to the China Southwest Architectural Design and Research Institute Corporation, Ltd., for supplying the test specimens.

Conflicts of Interest: The authors declare no conflict of interest.

References

- Xu, W.; Chen, D.; Qian, H.; Chen, W. Non-uniform temperature field and effects of large-span spatial truss structure under construction: Field monitoring and numerical analysis. *Structures* **2020**, *29*, 416–426. [\[CrossRef\]](#)
- Zhang, Q.; An, Y.; Zhao, Z.; Fan, F.; Shen, S. Model selection for super-long span mega-latticed structures. *J. Constr. Steel Res.* **2018**, *154*, 1–13. [\[CrossRef\]](#)
- El-Sheikh, A. Development of a new space truss system. *J. Constr. Steel Res.* **1996**, *37*, 205–227. [\[CrossRef\]](#)
- Shen, S.Z.; Lan, T.T. A Review of the Development of Spatial Structures in China. *Int. J. Space Struct.* **2001**, *16*, 157–172. [\[CrossRef\]](#)
- Tan, Y.; Zhang, Y.; Zhang, Q.; Fan, F. Static properties and stability of super-long span aluminum alloy mega-latticed structures. *Structures* **2021**, *33*, 3173–3187. [\[CrossRef\]](#)
- He, Y.; Zhou, X. Static properties and stability of cylindrical ILTDBS reticulated mega-structure with double-layer grid substructures. *J. Constr. Steel Res.* **2007**, *63*, 1580–1589. [\[CrossRef\]](#)
- Zhou, X.; He, Y.; Xu, L. Formation and stability of a cylindrical ILTDBS reticulated mega-structure braced with single-layer latticed membranous shell substructures. *Thin-Walled Struct.* **2009**, *47*, 537–546. [\[CrossRef\]](#)
- Zhou, X.; He, Y.; Xu, L. Stability of a cylindrical ILTDBS reticulated mega-structure with single-layer LICS substructures. *J. Constr. Steel Res.* **2009**, *65*, 159–168. [\[CrossRef\]](#)
- Ye, Y.-Y.; Liang, S.-D.; Feng, P.; Zeng, J.-J. Recyclable LRS FRP composites for engineering structures: Current status and future opportunities. *Compos. Part B Eng.* **2021**, *212*, 108689. [\[CrossRef\]](#)
- Yildiz, K.; Gürkan, I.; Turgut, F.; Cebeci, F.; Cebeci, H. Fracture toughness enhancement of fuzzy CNT-glass fiber reinforced composites with a combined reinforcing strategy. *Compos. Commun.* **2020**, *21*, 100423. [\[CrossRef\]](#)
- Wan, Y.; Yao, J.; Li, H.; Huang, Y.; You, P.; Xu, Y.; Lei, Z. Experimental studies of low-velocity impact behavior on hybrid metal wire net/woven carbon-fiber reinforced composite laminates. *Compos. Commun.* **2022**, *32*, 101185. [\[CrossRef\]](#)
- Dong, Z.; Han, T.; Zhang, B.; Zhu, H.; Wu, G.; Wei, Y.; Zhang, P. A review of the research and application progress of new types of concrete-filled FRP tubular members. *Constr. Build. Mater.* **2021**, *312*, 125353. [\[CrossRef\]](#)
- Ozbakkaloglu, T.; Xie, T.Y. Geopolymer concrete-filled FRP tubes: Behavior of circular and square columns under axial compression. *Compos. Part B Eng.* **2016**, *96*, 215–230. [\[CrossRef\]](#)
- Yan, Z.; Pantelides, C.P.; Reaveley, L.D. Posttensioned FRP composite shells for concrete confinement. *J. Compos. Constr.* **2007**, *11*, 81–90. [\[CrossRef\]](#)
- Siddiqui, N.A.; Alsayed, S.H.; Al-Salloum, Y.A.; Iqbal, R.A.; Abbas, H. Experimental investigation of slender circular RC columns strengthened with FRP composites. *Constr. Build. Mater.* **2014**, *69*, 323–334. [\[CrossRef\]](#)
- Bhowmik, T.; Tan, K.H.; Balendra, T. Lateral load-displacement response of low strength CFRP-confined capsule-shaped columns. *Eng. Struct.* **2017**, *150*, 64–75. [\[CrossRef\]](#)
- Li, F.; Zhao, Q.; Chen, L.; Shao, G. Experimental and theoretical research on the compression performance of CFRP sheet confined GFRP short pipe. *Sci. World J.* **2014**, *2014*, 1–12. [\[CrossRef\]](#) [\[PubMed\]](#)
- Correia, M.M.; Nunes, F.; Correia, J.R.; Silvestre, N. Buckling behavior and failure of hybrid fiber-reinforced polymer pultruded short columns. *J. Compos. Constr.* **2013**, *17*, 463–475. [\[CrossRef\]](#)
- Guares, E.; Aravinthan, T.; Islam, M. Characterisation of the mechanical properties of pultruded fibre-reinforced polymer tube. *Mater. Des.* **2014**, *63*, 305–315. [\[CrossRef\]](#)
- Cardoso, D.C.; Harries, K.A.; Batista, E.D.M. Compressive strength equation for GFRP square tube columns. *Compos. Part B Eng.* **2014**, *59*, 1–11. [\[CrossRef\]](#)

21. Fanggi, B.L.; Ozbakkaloglu, T. Behavior of hollow and concrete-filled FRP-HSC and FRP-HSC-steel composite columns subjected to concentric compression. *Adv. Struct. Eng.* **2015**, *18*, 715–738. [[CrossRef](#)]
22. Cao, Q.; Tao, J.; Wu, Z.; Ma, Z.J. Behavior of FRP-steel confined concrete tubular columns made of expansive self-consolidating concrete under axial compression. *J. Compos. Constr.* **2017**, *21*, 04017037. [[CrossRef](#)]
23. Zhou, Y.; Liu, X.; Xing, F.; Li, D.; Wang, Y.; Sui, L. Behavior and modeling of FRP-concrete-steel double-skin tubular columns made of full lightweight aggregate concrete. *Constr. Build. Mater.* **2017**, *139*, 52–63. [[CrossRef](#)]
24. Zhang, B.; Teng, J.G.; Yu, T. Compressive behavior of double-skin tubular columns with high-strength concrete and a filament-wound FRP Tube. *J. Compos. Constr.* **2017**, *21*, 04017029. [[CrossRef](#)]
25. Al-Saadi, A.U.; Aravinthan, T.; Lokuge, W. Structural applications of fibre reinforced polymer (FRP) composite tubes: A review of columns members. *Compos. Struct.* **2018**, *204*, 513–524. [[CrossRef](#)]
26. Zureick, A.; Scott, D. Short-term behavior and design of fiber-reinforced polymeric slender members under axial compression. *J. Compos. Constr.* **1997**, *1*, 140–149. [[CrossRef](#)]
27. Qian, P.; Feng, P.; Ye, L. Experimental study on GFRP pipes under axial compression. *Front. Struct. Civ. Eng.* **2008**, *2*, 73–78. [[CrossRef](#)]
28. Godat, A.; Légeron, F.; Gagné, V.; Marmion, B. Use of FRP pultruded members for electricity transmission towers. *Compos. Struct.* **2013**, *105*, 408–421. [[CrossRef](#)]
29. Wu, C.; Tian, J.; Ding, Y.; Feng, P. Axial compression behavior of pultruded GFRP channel sections. *Compos. Struct.* **2022**, *289*, 115438. [[CrossRef](#)]
30. Ding, L.; Liu, X.; Wang, X.; Huang, H.; Wu, Z. Mechanical properties of pultruded basalt fiber-reinforced polymer tube under axial tension and compression. *Constr. Build. Mater.* **2018**, *176*, 629–637. [[CrossRef](#)]
31. Zhan, Y.; Wu, G.; Harries, K.A. Determination of critical load for global flexural buckling in concentrically loaded pultruded FRP structural struts. *Eng. Struct.* **2018**, *158*, 1–12. [[CrossRef](#)]
32. Chen, L.; Pan, D.; Zhao, Q.; Niu, L.; Cong, L.; Li, C. Overall buckling characteristics of slender FRP-foam sandwich tube under axial compression. *Compos. Commun.* **2020**, *24*, 100585. [[CrossRef](#)]
33. Zeng, J.-J.; Guo, Y.-C.; Liao, J.; Shi, S.-W.; Bai, Y.-L.; Zhang, L. Behavior of hybrid PET FRP confined concrete-filled high-strength steel tube columns under eccentric compression. *Case Stud. Constr. Mater.* **2022**, *16*, e00967. [[CrossRef](#)]
34. Wang, Y.; Zhong, Y.; Wan, B.; Zhang, B.; Wei, Z.; Bai, Y. Axial compressive behavior and modeling of fiber-reinforced polymer-concrete-steel double-skin tubular stub columns with a rectangular outer tube and an elliptical inner tube. *Eng. Struct.* **2022**, *260*, 114222. [[CrossRef](#)]
35. Zhang, C.; Li, Y.; Wu, J. Mechanical properties of fiber-reinforced polymer (FRP) composites at elevated temperatures. *Buildings* **2022**, *13*, 67. [[CrossRef](#)]

Disclaimer/Publisher's Note: The statements, opinions and data contained in all publications are solely those of the individual author(s) and contributor(s) and not of MDPI and/or the editor(s). MDPI and/or the editor(s) disclaim responsibility for any injury to people or property resulting from any ideas, methods, instructions or products referred to in the content.